Contributions to Geophysics and Geodesy Vol. 53/1, 2023 (43–63)

# Detection of subsurface basaltic sheets and associated structures utilising forward modelling and inversion of 2D electrical resistivity data: A case study from Jebel-Qatrani, Fayoum, Egypt

Muhammad A. EL HAMEEDY*, Walid M. MABROUK, Said DAHROUG, Ahmed M. METWALLY

Department of Geophysics, Faculty of Science, Cairo University, Giza, Egypt

**Abstract:** In the north of Fayoum Governate, Egypt, numerous extrusive flows of basalt rocks exposed on the surface and affected by weathering and erosion, forming altered basalt sheets which is the case of the Jebel-Qatrani. The study objective comes in two main folds: the first, to choose the optimum parameters required for the filed survey by generating forward models using several arrays with 3% Gaussian random noise, simulating the geology of the study area deploying a finite element modelling approach; the second, to acquire the real field data and generate the electrical resistivity tomograms to ascertain the existence, extension, and characteristics of the basaltic sheets in the subsurface. Hence, four electrical resistivity profiles with a Wenner-alpha array with 48 electrodes, 5 metre electrode spacing, and a total length of 235 metres were acquired in suitable locations based on previous aeromagnetic results in the vicinity of the study area. These profiles were inverted to derive the true resistivity distribution of the subsurface. Another objective is to detect the near-surface, Oligocene normal faulting structures associated with rifting of the Red Sea. Results from two inverted resistivity tomograms show a possible normal fault cutting through the early Oligocene Qatrani Formation at the same time as red sea rifting, confirming previous geological studies in the Fayoum region based on satellite imagery, aeromagnetic data, and geological outcrops. It is concluded that near these faults, a sheet-like body of relatively high resistivity values, representing basaltic extrusions, was detected, confirming that the basaltic presence is associated with these structural zones.

**Key words:** forward modelling, inversion, Wenner array, basaltic sheet, ERT

## 1. Introduction

Several extrusive basalt flow outcrops have been studied, geologically, in recent decades due to their historical and economic significance. Several

*corresponding author, e-mail: mashraf@sci.cu.edu.eg

doi: 10.31577/congeo.2023.53.1.3 

basalt quarries were established there 4500 years ago during the 4th and 5th dynasties of the old kingdom of Egypt (*Harrell and Bown, 1995; Storemyr el al., 2003*) to pave many temples in Giza, Saqqara, Sahura, and Niuserra pyramids to symbolise Egypt's fertile and organically rich black land. The current need to understand the near-surface structural regime of Jebel-Qatrani and the detection of associated basaltic sheets there is important to preserve the historical heritage of this area and to study this new case of horizontal basaltic sheets.

Direct Current (DC) electrical technique is one of the oldest and well-known geophysical techniques among the non-invasive geophysical exploration techniques, mainly because it is rapid and cost-effective. The most important advantage is that it is a non-destructive technique. The early application of the electric technique was made almost entirely by the early work of Conrad Schlumberger (*Schlumberger, 1912*) and Frank Wenner (*Wenner, 1912*). Since then, the electrical resistivity method has been widely used for mining studies (*Embeng et al., 2022; Horo et al., 2021; Busato el al., 2019*), hydrogeological studies (*Altmeyer et al., 2021; Petit et al., 2021*), environmental studies, especially in contaminant monitoring (*Trento et al., 2021; Morita et al., 2020*), engineering applications (*Guo et al., 2022; Lapenna and Perrone, 2022; Saha et al., 2022*), and archaeological investigations (*Milo et al., 2022; Gaber et al., 2021; Tezel and Alp, 2021*).

Many geophysical studies for the objective of fault mapping using ERT data in different geological settings and lithologies (*Ho et al., 2022; Arjwech et al., 2021; Bufford et al., 2012, Gélis et al., 2010*) are well developed. *Hyndman and Drury (1977)* investigated the physical properties of 87 basalt samples, including electrical resistivity (approx. 220 Ω.m), thermal conductivity, and shear wave velocity. Generally, this response is dependent on many factors such as lithology, degree of fracturing, saturation, fluid salinity, and clay content (*Lashkaripour et al., 2005*). *Mostafa et al. (2003)* studied the temperature dependence of the electrical resistivity of basalt and granite samples from several localities bearing those sheets in Egypt. *Elhussein and Shokry (2020)* studied the occurrence of Oligocene basalt in the Egyptian western desert using airborne magnetic data and to delineate basalt edges and extensions in the subsurface.

The current work is aimed at highlighting the efficiency of the 2-D Electrical Resistivity Tomography (ERT) technique to detect the basaltic sheets

and associated fault structures and also to study the electrical resistivity response of sheet-like basaltic bodies using ERT tomograms.

The present paper is divided into four main sections. The geological context of the Jebel-Qatrani study area is discussed in Sect. 2. In this section, we also present the available geophysical datasets that are relevant for this site and the processing of this geophysical data. Section 3 examines the effectiveness of forward modelling to choose appropriate acquisition parameters for detecting basaltic flow in the shape of a horizontal sheet and faulted sheet. Three arrays were tested: Wenner-alpha, Schlumberger, and Dipole-Dipole arrays. Then these models were inverted to get the true electrical resistivity tomography (ERT) sections. In the next step we worked with real data from the site and inverted it to interpret the results in Sect. 4. From this data, we delineated the position of two faults. The presence of these faults is discussed in light of all the available data.

## 2. Geologic setting of the area

The study area is located at the north of the Fayoum depression in Fig. 1a, in the northern Western Desert of Egypt, and lies between latitudes 29.749089° and 29.735839° and between 30.702895° and 30.728082° longitudes, with four electrical resistivity profiles as shown in Fig. 1b and a surface topography generally dipping southward.

Several basalt sheets are exposed near the study area as in Fig. 1c due to the presence of extrusive basalt cover on top of Jebel-Qatrani (Jebel-Qatrani can be translated from Arabic as Tar Hills). This basalt occurs in several localities all over Egypt, mainly at Gabal Qtrani, Cairo-Suez District, south Quseir, Abu Zaabal, Baharyia Oasis, East Samalut, and south Wadi Hodein and is considered the youngest unit in the basement rocks in Egypt (*Shahin and Masoud, 2013*).

The most important study of Oligocene basalts was done by (*Abdel Meguid et al., 1992*), who classified the Tertiary basalts found in the Jebel Qatrani, South Quseir, and East Samart regions into two main types: high $TiO_2$ basalt and low $TiO_2$ basalt. He also concluded that the intraplate continental basaltic volcanism that produced the Tertiary basalts common in Egypt was contemporaneous with the opening of the Red Sea and the uplift of the African-Arabian dome.

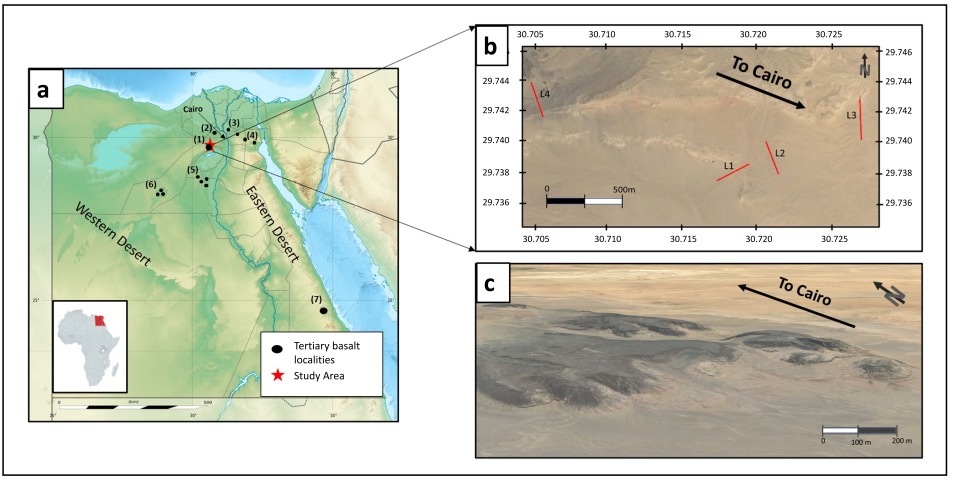


Fig. 1. (a) Relief map of Egypt displaying the study area (marked as a red star) and intraplate basalt intrusions (as black circles); (b) areal imagery (*Google Earth, 2021a*) displaying the locations of the profiles conducted in the area; and (c) areal imagery (*Google Earth, 2021b*) illustrating exposed basaltic sheets a few kilometres to the south-west of the surveyed area (Widan el-Faras area).

## 2.1. Stratigraphy

The study area is covered by a variety of sedimentary rocks ranging in age from the Oligocene to the Miocene. The Qatrani Formation (Oligocene) was deposited over the Qasr El Sagha Formation (Eocene). These two formations are exposed as large scarps on the northern and eastern sides of the Fayoum depression (Fig. 2), dominated by a relatively thick siliclastic sedimentary sucession (*Said, 1962*).

Two members of the Qatrani Formation (Fm) can be recognised and were first described by *Beadnell (1905)*. To the southwest of the study area, the lower member can be recognised, while the upper member is recognised at our study area at Jebel-Qatrani as sandstone with clay interbeds. The depositional environment of Qatrani Fm is a complex alluvial unit which facies changes laterally and vertically at both small and large scales and extends to a maximum thickness of 250 m.

*Beadnell (1905)* described Tertiary (Oligo-Miocene) basalts in the Fayoum depression as sheets and flows subdivided into three units from top to bottom as follows: altered basalt layer rich in cavities filled with halite and

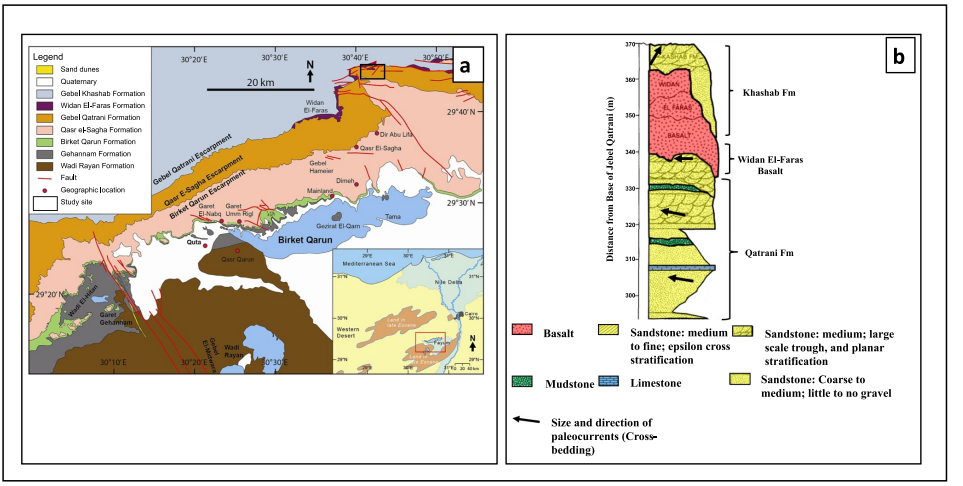


Fig. 2. (a) Geological map of northern Fayoum province modified after (*El Baz et al., 2022*); (b) lithostratigraphic description of the outcrop in the study area.

secondary calcite pockets; basalt rich in vesicles which are filled with calcite and sulfur; olivine basalt ranging from very hard to fractured basalt filled with sulfur. These basalt lavas cover the upper Qatrani cliffs with varying thicknesses from 2 to 25 m. (The latter thickness is recorded at Widan El Faras, Fig. 1) (*El-Hinnawi et al., 2021*), at the outcrops where basalt is thinnest, there appears to be a single flow; however, some authors believe that there are two or more flows (*Bown et al., 1988; Fleagle et al., 1986*).

Khashab Formation of Miocene age overlaying Widan el Faras basalt consists mainly of coarse sandstone, cobble conglomerate, and chert-bebble with petrified wood fragments disseminated on the surface. Many outcrops around the study area of Jebel-Qatrani were studied and concluded in Fig. 2.

## 2.2. Structural setting

At the end of the Oligocene, a tensional tectonic episode occurred and was accompanied by northwest-trending normal faults throughout the northern parts of the Eastern and Western Deserts of Egypt. Basaltic lava has extruded from these cracks in different places (*Rittmann, 1954*). Many authors investigated the Fayoum fault system in order to learn more about the ori-

gins of the Fayoum depression (*Kusky et al., 2011; Said, 1979; Bayoumi and Gamili, 1970; Blankenhorn, 1901*). The Jebel-Qatrani volcanic rocks were assumed to be related to the extensional phase of Red Sea opening (*El-Shazly et al., 1974*). A main goal of this study is to delineate these normal faults.

The major fault trends in the area (Fig. 2) are NW–SE (Clysmic trend) and E–W (Tethyan trend). Near the northern part of the study area, an E–W strike-slip fault offsets the basaltic sheets there by about 2 km. In the eastern part of the Jebel-Qatrani area (*Alrefaee and Abd el-aal., 2017*), they detected some active faults, and this supports that the neo-tectonic activity in the Fayoum area is one of the most important factors to put into consideration before any development plans in the area.

### 2.3. Data sources and processing

In this paper, we used the Res2dmod software to generate synthetic data, which was then exported as model files, inverted with Res2dinv, and displayed as 2D electrical resistivity tomographs.

The field dataset in Fig. 3 was gathered using an IRIS Syscal Pro résistivimètre based on aeromagnetic data results collected over the Fayoum

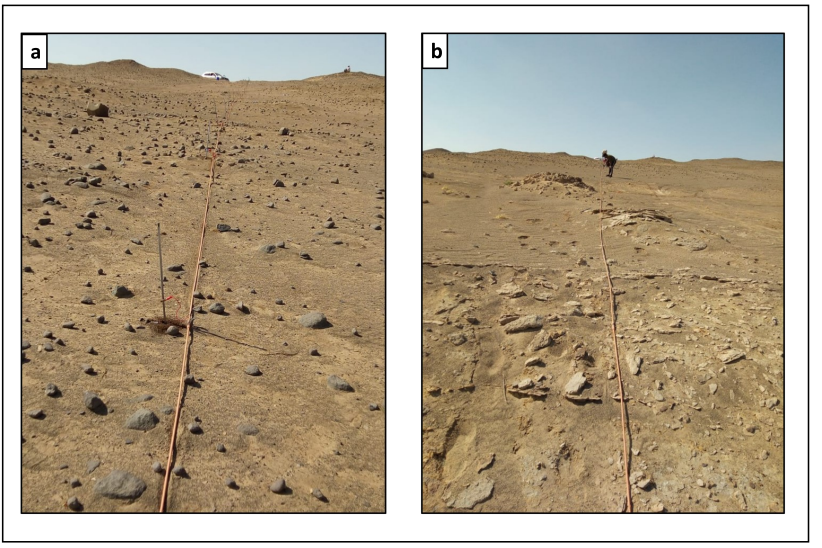


Fig. 3. Field data acquisition along (a) profile L-2, and (b) profile L-3.

province. Two electric cable reels were used to extend the length of the profile to 235 m. The Wenner array was selected based on results of numerical models in Sect. 3 with a maximum depth of approximately 38 m using 48 electrodes and a 5 m electrode spacing.

The field topography data were imported, and the measured data points were examined to look for errors (bad data points). Profile L-3 and L-4 indicate some bad data points, so they were removed. Then the field data was exported as Res2dinv data files with topography embedded within the data files.

Aeromagnetic data acquired over Fayoum province was utilised to determine the location of ERT profiles. Fig. 4 represents the Tilt Derivative (TDR) filter map of the Reduced to North Pole (RTP) after (*Abdel Kader et al., 2013*) for the same dataset overlaid by the study area locations.

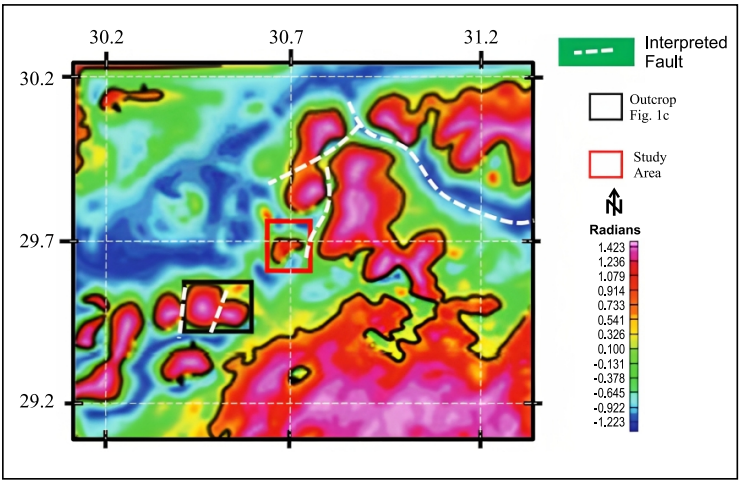


Fig. 4. Tilt Derivative Map (TDR) of the Reduced to the Pole (RTP) for Fayoum province showing several anomalies representing basaltic sheets. The black lines represent the zero-contour lines of (TDR), which is at or near the position of contact. Modified after *Abdel Kader et al. (2013)*.

The Tilt Derivative filter (TDR) has been applied to magnetic data, where contact locations can be easily tracked on a map (*Salem et al., 2008*). Figure 4 highlights relatively small anomalies present within the study area representing near basaltic sheets. The nearby exposed sheet in Fig. 1 is also detected in the (TDR) aeromagnetic map.

## 3. Methodology

### 3.1. Numerical modelling

Three theoretical apparent resistivity psedusections were produced for a model with three arrays. Based on studying outcrops in the area of study and the predicted subsurface structures Wenner-alpha, Schlumberger, and Dipole-Dipole presented in Fig. 5 were tested. The generated synthetic model is a faulted basaltic sheet-like body of 800 Ω.m with a surface topography simulating field topography embedded within alluvial sediments of 30 Ω.m of host rock overlain by 200 Ω.m of sandstone with petrified wood fragments.

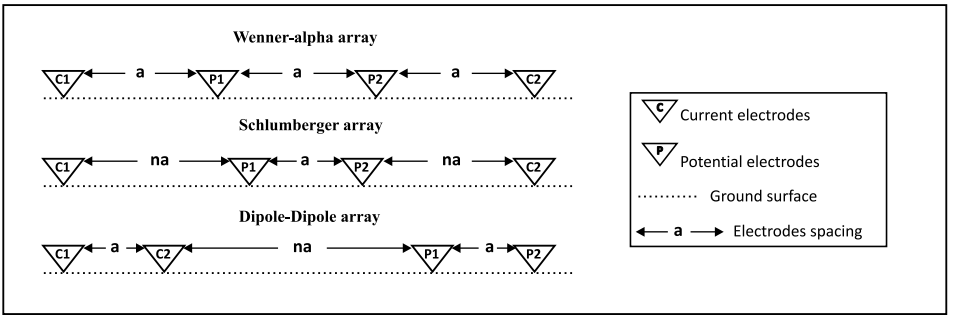


Fig. 5. Most common arrays for 1D, 2D, 3D electric profiling and sounding.

In this paper, the authors utilised (Res2dmod) software to generate several numerical models (Fig. 6), to choose the optimum survey parameters. The constructed model of resistivity distribution in Fig. 6 was constructed based on geological outcrop studies conducted at several locations where the basalt is exposed on the surface, and the depth to the basalt in the study area was chosen based on drilling data from modern basalt quarry activities, before declaring the area a historical heritage area.

Generally, these apparent resistivity models are divided into small elements of (structured and unstructured), (quadrilateral and triangular), and (homogenous and isotropic) cells, which produce a numerical model to be solved either with the finite difference method (*Dey and Morrison, 1979; Loke and Barker, 1996*) or the finite element method (*Smith and Vozzof, 1984*). The latter is our case with a quadrilateral structured mesh contaminated with 3% Gaussian random noise. The modelled apparent resistivity data in Fig. 6 are inverted using the least square inversion algorithm in

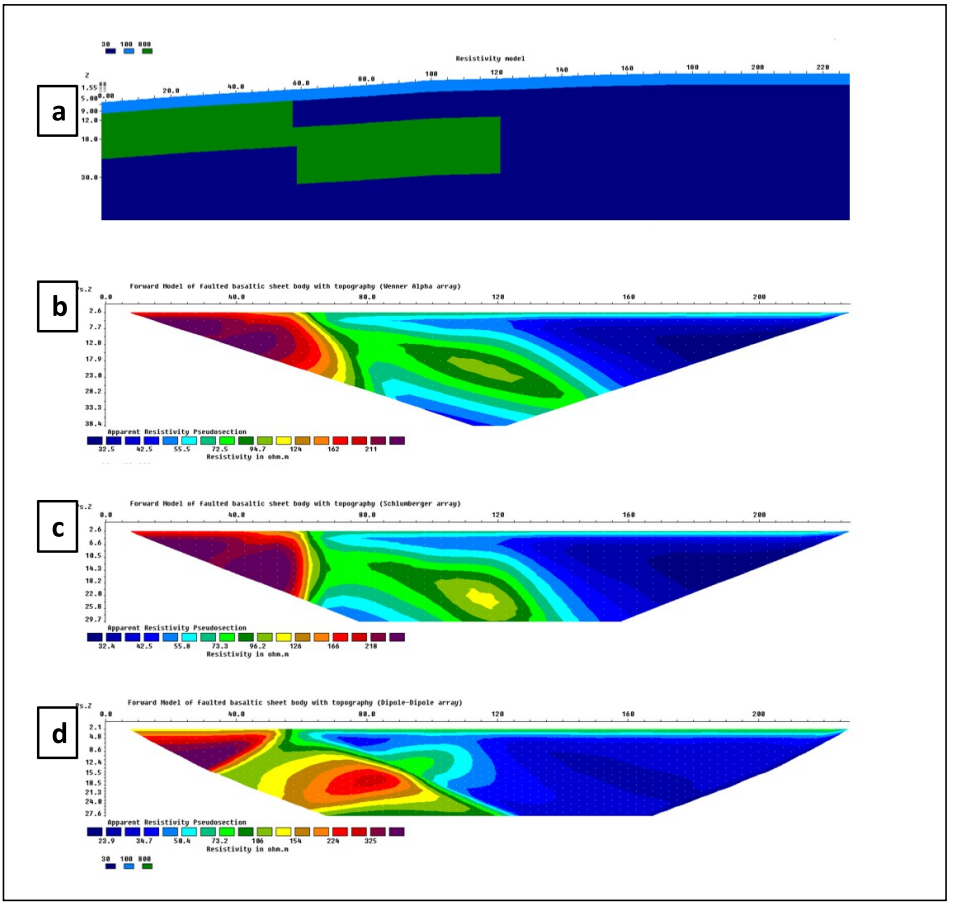


Fig. 6. Forward Modelling results for (a) faulted basaltic sheet with surface topography simulating a study area show the apparent resistivity distribution of the subsurface for (b) Wenner-alpha array, (c) Schlumberger array, and (d) Dipole-Dipole array.

(Res2dinv) tomographic inversion. The results of these scenarios are synthetic datasets, which are simplified representations of the subsurface resistivity structure of the geologic setting within the studied area.

It is worth noting that sensitivity analysis of the used arrays and more is well-studied and there are good examples (*Qiang et al., 2022; Wilkinson et al., 2012; Dahlin and Zhou, 2004; Furman et al., 2003*) of optimization algorithms for obtaining an optimised measurement configuration based on the model resolution matrix. *Singh and Sharma (2022)* performed to study

the sensitivity and geometric factors of the same three arrays used here. However, the topic of sensitivity analysis is out of scope for the current case study, and the numerical simulations were to coarsely define the parameters to just initiate the first phase of the site studies, and future studies in this area will be initiated based on the results from the current research.

### 3.2. Inversion

From apparent resistivity psedusection acquired in the field or computed theoretically, the inversion is employed to obtain the true resistivity structure of the subsurface. Each iteration of the inversion scheme can be broken down into three steps (*Loke and Barker, 1995*):

- The first step is calculating the apparent resistivity for a model we have been building using finite-element or finite difference methods in which we divide the subsurface into small cells, and those cells normally increase in size with depth (*Dahlin, 2001*). In this paper, we used the forward model subroutine with the finite element method because it is more flexible, especially when there is topography present in the model. The difference between calculated and measured apparent resistivity is used to determine the (RMS) error between them.
- Secondly, the Jacobian matrix of partial derivatives is calculated. Using Gauss-Newton or quasi-Newton methods (*Loke and Dahlin, 2002*), the Gauss-Newton method requires more time to calculate the Jacobian matrix but gives better results than the quasi-Newton method, especially if high contrast in resistivity is present, and the Gauss-Newton method has been used for numerical simulations.
- Finally, the least-square equation has to be solved where Gauss-Newton or Quasi-Newton methods are used in this equation to be solved. Generally, the inversion of 2D and 3D resistivity data is carried out using the regularised least-square optimization method mentioned previously. To constrain this optimization, two methods are used:
    1. Least-squares method with smoothness constraints (L2 norm) (*deGroot-Hedlin and Constable, 1990*).
    2. Blocky constrained least-square method (L1 norm) (*Claerbout and Muir, 1973*).

The choice of one over the expanse of the other depends on the nature of the subsurface resistivity changes. If the change is gradual and there are no sharp boundaries, it is preferred to use smooth inversion. But the blocky inversion method gives significant results when there are sharp boundaries (*Loke et al., 2003*) – there are relatively high abrupt changes in resistivity at boundaries.

Overestimation of the thickness of the basaltic sheet in the solution of the tested arrays is most likely related to the smoothing constraint employed as part of the regularisation process in the inversion scheme (*Marescot et al., 2004; Carey et al., 2017*). The generated numerical simulations used in this paper were inverted using the smoothness constrained least-square method (L2 norm).

The Wenner-alpha array is sensitive to vertical variations in resistivity, so it can identify horizontal structures better than the Dipole-Dipole array, which has greater sensitivity to lateral variations in resistivity, so it can identify horizontal structures. In the Dipole-Dipole array, the average value of artifacts is greater than expected by the synthetic model, and because of the nature of the D-D array in which the potential dipoles are located outside of the in-line current dipole (Fig. 5), it creates minor potential field gradients, which are hard to solve during the inversion, resulting in these significant artifacts.

Schlumberger array represents a middle ground between Wenner and Dipole-Dipole arrays with high sensitivity to define horizontal and vertical structures. The inversion results of the numerical simulations presented in Fig. 7 demonstrate a significant decrease in inversion artifacts in Wenner and Schlumberger than in the Dipole-Dipole array. Parameters and inversion results of numerical simulations are represented in Table 1.

Table 1. Synthetic model characteristics and inversion results of faulted sheet model.

| Array | No. data points | No. electrodes | Electrodes spacing (m) | RMS error (%) | No. iterations | Dipole length in meters (a) | Separation factor (n) |
|---|---|---|---|---|---|---|---|
| Wenner-alpha | 357 | 48 | 5 | 4.2 | 6 | 5,10,15,...,70 | – |
| Schlumberger | 465 | 48 | 5 | 3.9 | 5 | 5 | 1–15 |
| Dipole-Dipole | 570 | 48 | 5 | 3.1 | 5 | 5 | 1–15 |

In general, while deciding between electrical resistivity arrays, the acquisition time factor is a significant aspect to take into consideration, along with its ability to define the boundaries of the basaltic sheet, as well as the ability of the array chosen to give the lowest inversion artifacts.

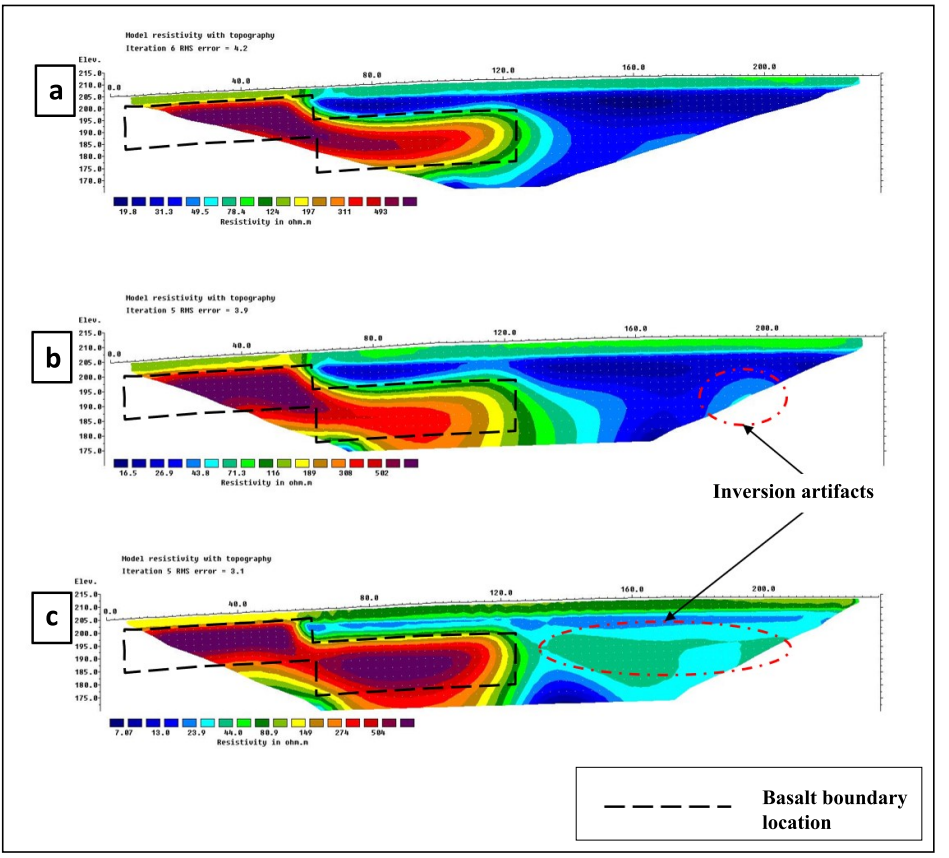


Fig. 7. Inversion results of theoretical data generated in Fig. 6. (a) Inverted Resistivity tomogram for Wenner-alpha array; (b) Schlumberger array, and (c) Dipole-Dipole array.

### 3.3. Application to field data

Application to real data aims to assess the lithology of the subsurface and calculate the thickness of the basalt sheet for various purposes, as well as outline the extent of this sheet, by integrating forward modelling and field

investigation results. 2D ERT field dataset were inverted using Res2dinv inversion algorithm. The algorithm of Res2dinv is a non-linear optimization technique used to determine the subsurface resistivity distribution using two inversion schemes. The first one named a normal scheme (L2 norm, smoothed least square constraint) and the second one named robust scheme or blocky inversion (L1 norm smoothed constrains).

In this paper we used the standard least square inversion (L2 norm), which results in a small RMS error, which is the minimization of the square of the difference between the measured and the calculated apparent resistivity. The inversion process stopped when the improvement in the RMS error was not significantly large. The field data exhibits an RMS error range of 1.3 % to 7.7 % after 6 to 7 iterations as shown in Table 2.

Table 2. Field data parameters and inversion results.

| Profile No. | Inversion | No. data points | Dipole length in meters (a) | No. electrodes | Electrodes spacing (m) | RMS error (%) | No. iterations |
|---|---|---|---|---|---|---|---|
| L-1 | Least square | 359 | 5,10,15,...,75 | 48 | 5 | 5.7 | 6 |
| L-2 | Robust* | 360 | 5,10,15,...,75 | 48 | 5 | 1.3 | 7 |
| L-3 | Least square | 330 | 5,10,15,...,75 | 48 | 5 | 7.7 | 7 |
| L-4 | Least square | 357 | 5,10,15,...,75 | 48 | 5 | 3.8 | 6 |

*Note: The robust inversion scheme was used in the inversion of profile-2 because it gave lower error than the least square inversion scheme.

## 4. Results and discussion

The uppermost layer, consisting of dry sandstone from offset 0 to 100 metres and reaching a depth of 5 metres, and alluvium with relatively low resistivity ranging from 100–235 m and exposed at surface, was recognised across the profile, according to the inversion results of the geoelectric section of profile L-1 calculated by the Wenner-alpha array (Fig. 8a).

At 3–6 metres depth, a noticeable, resistive zone of more than 120 Ω.m is discernible. This feature indicates a fractured and weathered basaltic sheet with low resistivity values (130 Ω.m) affected by the E–W Oligocene-Quaternary faulting system and filled with auxiliary halite based on the sig-

nificant resistivity differences and aeromagnetic anomalies from data gathered across this area. Several drainage patterns cut through surface sediments (small channels visible in Fig. 1) which transport water and clay during rainy days through the Miocene Khashab sandstone formation and Oligocene Qatrani alluvial sediments, infiltrating the fractured basalt and lowering its resistivity values.

The sharp interface between the basalt boundary, with an average thickness of 15 m, and the host Qatrani formation can be identified, and this is due to the selection of the Wenner-alpha array, which proves its capability to delineate the basalt sheet effectively as proposed in Sect. 3.1.

Profile L-2 (Fig. 8b) oriented NW–SE shows the presence and extension of a basaltic body (resistive anomaly) overlaying Oligocene Qatrani Fm with a resistivity value of approx. 3200 Ω.m, which implies that this body is relatively intact and not heavily weathered or fractured. A nearly vertical heterogeneity feature is interpreted as a fracture zone located at $x = 185$ m related to the extrusion and occurrence of this Oligocene basalt. A blocky constrained least-square inversion routine (L1) was applied for profile L-2 inversion because it gave minimum RMS error and worked very well in the case of sharp boundaries of intact resistive basalt (3200 Ω.m) and less resistive (30 Ω.m) alluvium sediments.

Inversion results of profile L-3 oriented almost N–S, which is an illustration of a major fault structure within the study area that is interpreted as a fault related to the E–W fault system, which displaced nearby exposed basaltic bodies 2 km away from each other.

Finally, Profile L-4 (Fig. 8d) shows an extreme case in which the basalt was exposed to the surface and exploited within ancient Egypt. Beneath the basalt, the Qatrani formation is present with a thickness of 10–25 m and is affected by a possible fault.

Based on both synthetic and field data from profiles L-1 to L-4, the results support that the horizontal structures are delineated quite well in 2D geoelectric sections measured by the Wenner-alpha array agreeing (*Dahlin and Zhou, 2006*) work of sensitivity analysis. The selection of this array was made due to its effectiveness in investigating regions with vertical resistivity variations.

Academically, each type of array has advantages and drawbacks because investigating subsurface geological characteristics with more than one ar-

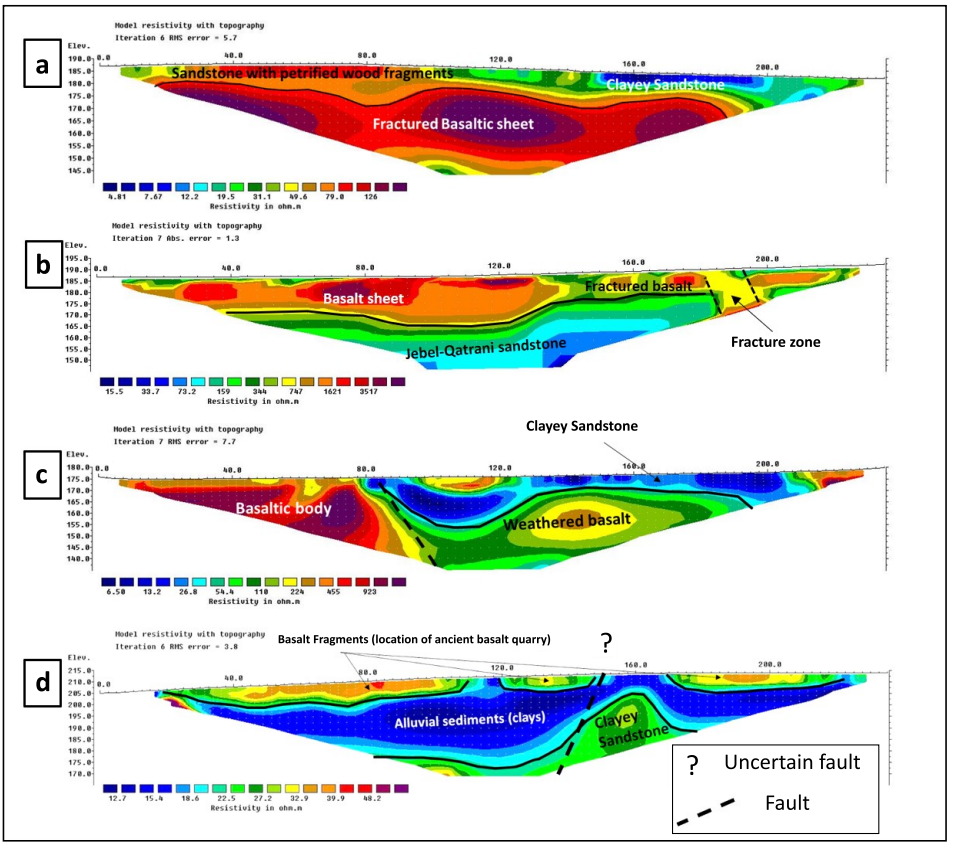


Fig. 8. Inversion results of field data (Fig. 1b) using Res2dinv: (a) Profile L-1 shows relatively low resistivity Fractured basaltic layer; (b) Interpreted fracture zone and high resistivity intact basaltic sheet in profile L-2; (c) Profile L-3 with a major fault associated with basalt intrusion during the Oligocene; (d) Profile L-4 at the top of Jebel Qatrani along ancient basalt quarry with very low resistivity response due to water infiltration and fracturing in the extrusive sheet at the top of Mountain Qatrani.

ray at the same location may result in different geoelectrical inverse models due to inconsistent conceptual and inherited applied benefits and drawbacks (*Athanasiou et al., 2007*). However, in our situation and based on the numerical simulations, the Wenner array worked well. The current work was done on an exploratory basis, and this suggests that the resistivity imaging approach may identify the basaltic sheet from the surrounding rocks in such ancient mining locations.

## 5. Conclusion

The results of this research demonstrate how ERT may be utilised to examine subsurface extrusive basalt sheets within a sedimentary alluvial environment and associated faults, taking into account the surface geology and regional structural setting.

Numerical models used in this paper were utilised to confirm the applicability of the Wenner-alpha array in detecting and delineating—effectively—the basaltic sheet boundaries mounted in less resistive alluvial sediments host rock and to choose the optimum survey parameters. The Wenner array proved that it is the most suitable array for the problem at hand, with the ability to delineate horizontal structures (basaltic-sheet) with minimum inversion artifacts relative to Dipole-dipole and Schlumberger arrays, and the apparent resistivity anomaly is closely matched to the location of the subsurface sheet with its location, extent, and size since the Wenner-alpha array has better vertical resolution. Furthermore, the number of data points relative to the other arrays is generally lower and leads to minimising acquisition time, which is a very important factor in any geophysical survey.

Furthermore, the Wenner-alpha array was used to conduct the field investigation along four lines. The geoelectrical resistivity tomographs that have been inverted reveal that the basaltic flow is forming a layer that caps the Oligocene Qatrani formation, which is associated with normal faults in the study area and shown as resistivity contrasts mounted within a complex alluvial depositional environment. Such sheet-like basaltic bodies were at a depth of 0.5–6 metres ranging in resistivity from 130–3000 Ω.m depending on the degree of weathering, fracturing, alteration, and rainwater infiltration through these fractures with the presence of auxiliary halite in this vesicular basalt. In future studies in the same area, this technique proposed here may help us obtain more accurate quantitative information from other geophysical methods to conceptualize the geological setting of this historical site.

***Author contributions.*** All authors contributed to the study conception and design. Material preparation, data collection and analysis were performed by Ahmed M. Metwally. The first draft of the manuscript was written by Muhammad Ashraf El Hameedy and all authors commented on previous versions of the manuscript. All authors read and approved the final manuscript.

***Declarations***.

- **Funding**: No funding was received.
- **Financial interests**: The authors declare they have no financial interests.
- **Non-financial interests**: none.

All authors certify that they have no affiliations with or involvement in any organization or entity with any financial interest or non-financial interest in the subject matter or materials discussed in this manuscript.

## References

Abdel Kader A. K., Kordik P., Khalil A., Mekkawi M., El-Bohoty M., Rabeh T., Khalil Refai M., El-Mahdy A., 2013: Interpretation of Geophysical Data at EL Fayoum—Dahshour Area, Egypt Using Three Dimensional Models. Arab. J. Sci. Eng., **38**, 7, 1769–1784, doi: 10.1007/s13369-012-0385-0.

Abdel Meguid A. A., El Metwally A. A., Morsy M. A., 1992: Tectonic evolution of continental basalts of Egypt: geochemical evidences. Egypt. Mineral., **4**, 141–158.

Alrefaee H. A., Abd el-aal A. K., 2017: Tectonic deformation and subsurface active fault trends of El-Faiyum province, Egypt as deduced by seismicity and potential field data. Arab. J. Geosci., **10**, 24, 547, doi: 10.1007/s12517-017-3326-0.

Altmeyer M., Seeliger M., Ginau A., Schiestl R., Wunderlich J., 2021: Reconstruction of former channel systems in the northwestern Nile Delta (Egypt) based on corings and electrical resistivity tomography (ERT). E&G Quat. Sci. J., **70**, 151–164, doi: 10.5194/egqsj-70-151-2021.

Arjwech R., Everett M. E., Chaisuriya S., Youngme W., Rattanawannee J., Saengchomphu S., Thitimakorn T., Somchat K., 2021: Electrical resistivity tomographic detection of the hidden Thakek fault, Northeast Thailand. Near Surf. Geophys., **19**, 4, 489–501, doi: 10.1002/nsg.12165.

Athanasiou E. N., Tsourlos P. I., Papazachos C. B., Tsokas G. N., 2007: Combined weighted inversion of electrical resistivity data arising from different array types. J. Appl. Geophys. **62**, 2, 124–140, doi: 10.1016/j.jappgeo.2006.09.003.

Bayoumi A. I., Gamili M. M., 1970: A Geophysical Study on the Fayum-Rayan Area, with References to Sub-surface Structures. 7th Arab. Petrol. Congress, Kuwait.

Beadnell H. J. L., 1905: The Topography and Geology of the Fayum Province of Egypt. Survey Department of Egypt, Cairo, 101 p.

Blankenhorn M., 1901: News on the Geology and Paleontology of Egypt: III. The Miocene (Neues zur Geologie und Paläontologie Aegyptens: III. Das Miozän). Z. Dtsch. Geol. Ges., **53**, 52–132 (in German).

Bown T. M., Kraus M. J., Wing S. L., Fleagle J. G., Tiffney B. H., Simons E. L., Vondra C. F., 1988: The Fayum Primate Forest Revisited. J. Hum. Evol., **11**, 7, 603–632, doi: 10.1016/S0047-2484(82)80008-0.

Bufford K. M., Atekwana E. A., Abdelsalam M. G., Shemang E., Atekwana E. A., Mickus K., Moidaki M., Modisi M. P., Molwalefhe L., 2012: Geometry and faults tectonic

activity of the Okavango Rift Zone, Botswana: Evidence from magnetotelluric and electrical resistivity tomography imaging. J. Afr. Earth Sci., **65**, 61–71, doi: 10.1016/j.jafrearsci.2012.01.004.

Busato L., Boaga J., Perri M. T., Majone B., Bellin A., Cassiani G., 2019: Hydrogeophysical characterization and monitoring of the hyporheic and riparian zones: The Vermigliana Creek case study. Sci. Total Environ., **648**, 1105–1120, doi: 10.1016/j.scitotenv.2018.08.179.

Carey A. M., Paige G. B., Carr B. J., Dogan M., 2017: Forward modeling to investigate inversion artifacts resulting from time-lapse electrical resistivity tomography during rainfall simulations. J. Appl. Geophys., **145**, 39–49, doi: 10.1016/j.jappgeo.2017.08.002.

Claerbout J. F., Muir F., 1973: Robust Modeling with Erratic Data. Geophysics, **38**, 5, 826–844, doi: 10.1190/1.1440378.

Dahlin T., 2001: The development of DC resistivity imaging techniques. Comput. Geosci., **27**, 9, 1019–1029, doi: 10.1016/S0098-3004(00)00160-6.

Dahlin T., Zhou B., 2004: A numerical comparison of 2D resistivity imaging with 10 electrode arrays. Geophys. Prospect., **52**, 5, 379–398, doi: 10.1111/j.1365-2478.2004.00423.x.

Dahlin T., Zhou B., 2006: Multiple-gradient array measurements for multichannel 2D resistivity imaging; Near Surf. Geophys. **4**, 2, 113–123, doi: 10.3997/1873-0604.2005037.

deGroot-Hedlin C., Constable S., 1990: Occam's inversion to generate smooth, two-dimensional models form magnetotelluric data. Geophysics, **55**, 12, 1613–1624, doi: 10.1190/1.1442813.

Dey A., Morrison F. H., 1979: Resistivity modeling for arbitrarily shaped three-dimensional structures, Geophysics, **44**, 4, 753–780, doi: 10.1190/1.1440975.

El Baz S. M., Wanas H. A., Abou Awad H. A., Assal E. M., 2022: Biostratigraphy, paleoecology, and paleobiogeography of the Middle–Late Eocene ostracods, north-west Fayoum area, Egypt. Geol. J., **57**, 9, 3686–3705, doi: 10.1002/gj.4496.

El Shazly E. M., Abdel Hady M. A., El Kassas I. A., El Shazly M. M., 1974: Geology of Sinai Peninsula from ERTS-2 Satellite Images. Remote Sensing Center, Cairo, 10 p.

El-Hinnawi E., Abayazeed S. D., Khalil A. S., 2021: Spheroidal weathering of basalt from Gebel Qatrani, Fayum Depression, Egypt. Bull. Natl. Res. Cent., **45**, 1, doi: 10.1186/s42269-020-00453-2.

Elhussein M., Shokry M., 2020: Use of the airborne magnetic data for edge basalt detection in Qaret Had El Bahr area, Northeastern Bahariya Oasis, Egypt. Bull. Eng. Geol. Environ., **79**, 9, 4483–4499, doi: 10.1007/s10064-020-01831-w.

Embeng S. B. N., Meying A., Ndougsa-Mbarga T., Moreira C. A., Owono Amougou O. U., 2022: Delineation and Quasi-3D Modeling of Gold Mineralization using Self-Potential (SP), Electrical Resistivity Tomography (ERT), and Induced Polarization (IP) Methods in Yassa Village, Adamawa, Cameroon: A Case Study. Pure Appl. Geophys., **179**, 2, 795–815, doi: 10.1007/s00024-022-02951-y.

Fleagle J. G., Bown T. M., Obradovich J. D., Simons E. L., 1986: Age of the earliest African anthropoids. Science, **234**, 4781, 1247–1249, doi: 10.1126/science.234.4781.1247.

Furman A., Ferré T. P. A., Warrick A. W., 2003: Sensitivity Analysis of Electrical Resistivity Tomography Array Types Using Analytical Element Modeling. Vadose Zone J., **2**, 3, 416–423, doi: 10.2136/vzj2003.4160.

Gaber A., Gemail K. S., Kamel A., Atia H. M., Ibrahim A., 2021: Integration of 2D/3D ground penetrating radar and electrical resistivity tomography surveys as enhanced imaging of archaeological ruins: A case study in San El-Hager (Tanis) site, northeastern Nile Delta, Egypt. Archaeol. Prospect., **28**, 2, 251–267, doi: 10.1002/arp.1810.

Gélis C., Revil A., Cushing M. E., Jougnot D., Lemeille F., Cabrera J., De Hoyos A., Rocher M., 2010: Potential of Electrical Resistivity Tomography to Detect Fault Zones in Limestone and Argillaceous Formations in the Experimental Platform of Tournemire, France. Pure Appl. Geophys., **167**, 11, 1405–1418, doi: 10.1007/s00024-010-0097-x.

Google Earth, 2021a: Google Earth Pro ver. 7.3.4.8248 (July, 2021): Jebel-Qatrani area, Northern Fayoum depression, Egypt. 29° 44′ 25.79″ N, 30° 42′ 56.50″ E, Eye alt 3.01 km, Maxar Technologies 2021 [Oct,6, 2022].

Google Earth, 2021b: Google Earth Pro ver. 7.3.4.8248 (July, 2021): Widan El-Faras basalt quarry, Northern Fayoum depression, Egypt. 29° 44′ 27.31″ N, 30° 42′ 56.36″ E, Eye alt 2.64 km, Maxar Technologies 2021 [Oct, 6, 2022].

Guo Y., Cui Y., Xie J., Luo Y., Zhang P., Liu H., Liu J., 2022: Seepage detection in earth-filled dam from self-potential and electrical resistivity tomography. Eng. Geol., **306**, 106750, doi: 10.1016/j.enggeo.2022.106750.

Harrell J. A., Bown T. M., 1995: An Old Kingdom Basalt Quarry at Widan el-Faras and the Quarry Road to Lake Moeris. J. Am. Res. Cent. Egypt, **32**, 71–91, doi: 10.2307/40000832.

Ho G.-R., Chang P.-Y., Lee J.-C., Lewis J. C., Chen P.-T., Hsu H.-L., 2022: Surface traces and related deformation structures of the southern Sanyi Fault, Taiwan, as deduced from field mapping, electrical-resistivity tomography, and shallow drilling. Eng. Geol., **273**, 105690, doi: 10.1016/j.enggeo.2020.105690.

Horo D., Pal S. K., Singh S., 2021: Mapping of Gold Mineralization in Ichadih, North Singhbhum Mobile Belt, India Using Electrical Resistivity Tomography and Self-Potential Methods. Mining Metall. Explor., **38**, 1, 397–411, doi: 10.1007/s42461-020-00340-4.

Hyndman R. D., Drury M. J., 1977: Physical properties of basalts, gabbros, and ultramafic rocks from DSDP Leg 37. In: Aumento F., Melson W. G., Hall J. M., Bougault H., Dmitriev L., Fischer J. F., et al. (Eds.): Initial reports of the Deep-Sea Drilling Project. **37**, 395–401, Washington, U.S. Government Printing Office, doi: 10.2973/DSDP.PROC.37.113.1977.

Kusky T. M., Ramadan T. M., Hassaan M. M., Gabr S., 2011: Structural and tectonic evolution of El-Faiyum depression, North Western Desert, Egypt based on analysis of

Landsat ETM+, and SRTM Data. J. Earth Sci., **22**, 1, 75–100, doi: 10.1007/s12583-011-0159-8.

Lapenna V., Perrone A., 2022: Time-Lapse Electrical Resistivity Tomography (TL-ERT) for Landslide Monitoring: Recent Advances and Future Directions. Appl. Sci., **12**, 3, 1425, doi: 10.3390/app12031425.

Lashkaripour M.,Ghafoori M.,Dehghani A., 2005: Electrical resistivity survey for predicting Samsor aquifer properties, southeast Iran. Geophys. Res. Abstr., **7**, 01999, European Geosciences Union.

Loke M. H., Barker R. D., 1995: Least-squares deconvolution of apparent resistivity psedusections. Geophysics, **60**, 6, 1682–1690, doi: 10.1190/1.1443900.

Loke M. H., Barker R. D., 1996: Rapid least-squares inversion of apparent resistivity pseudosections by a quasi-Newton method. Geophys. Prospect., **44**, 1, 131–152, doi: 10.1111/j.1365-2478.1996.tb00142.x.

Loke M. H., Dahlin T., 2002: A comparison of the Gauss-Newton and quasi-Newton methods in resistivity imaging inversion. J. Appl. Geophys., **49**, 3, 149–162, doi: 10.1016/S0926-9851(01)00106-9.

Loke M. H., Acworth I., Dahlin T., 2003: A comparison of smooth and blocky inversion methods in 2D electrical imaging surveys. Explor. Geophys., **34**, 3, 182–187, doi: 10.1071/EG03182.

Marescot L., Lopes S. P., Rigobert S., Piau J.-M., Humbert P., Lagabrielle R., Chapellier D., 2004: Forward and inverse resistivity modelling on complex three-dimensional structures using the finite element method. European Association of Geoscientists & Engineers, 17th EEGS Symposium on the Application of Geophysics to Engineering and Environmental Problems, cp-186-00053, doi: 10.3997/2214-4609-pdb.186.EEE06.

Milo P., Vágner M., Tencer T., Murín I., 2022: Application of Geophysical Methods in Archaeological Survey of Early Medieval Fortifications. Remote Sens., **14**, 10, 2471, doi: 10.3390/rs14102471.

Morita A. K. M., Pelinson N. S., Elis V. R., Wendland E., 2020: Long-term geophysical monitoring of an abandoned dumpsite area in a Guarani Aquifer recharge zone. J. Contam. Hydrol., **230**, 103623, doi: 10.1016/j.jconhyd.2020.103623.

Mostafa M. S., Afify N., Gaber A., Abozid E. F., 2003: Electrical Resistivity of Some Basalt and Granite Samples from Egypt. Egypt. J. Sol., **26**, 1, doi: 10.21608/EJS.2003.150009.

Petit A., Cerepi A., Le Roux O., Loisy C., Kennedy S., Estublier A., Noirez S., Garcia B., El khamlichi A., 2021: Study of Water Transfer Dynamics in a Carbonate Vadose Zone from Geophysical Properties. Pure Appl. Geophys., **178**, 6, 2257–2285, doi: 10.1007/s00024-021-02746-7.

Qiang S., Shi X., Xueyuan K., Revil A., 2022: Optimized arrays for electrical resistivity tomography survey using Bayesian experimental design. Geophysics, **87**, 4, E189–E203, doi: 10.1190/geo2021-0408.1.

Rittmann, A., 1954: Remarks on the eruptive mechanism of the tertiary volcanoes of Egypt. Bull. Volcanol., **15**, 1, 109–117, doi: 10.1007/BF02596000.

Saha A., Dey A. K., Kalita B., Vishwakarma S. P., Ahmed N., 2022: Prediction of Stability of Hill Slope Through Electrical Resistivity Tomography. In: Dey A. K., Mandal J. J., Manna B. (Eds.): Proceedings of the 7th Indian Young Geotechnical Engineers Conference. Lecture Notes in Civil Engineering, **195**, Springer, Singapore, doi: 10.1007/978-981-16-6456-4_31.

Said R., 1962: Geology of Egypt. Elsevier, Amsterdam, 377 p.

Said R., 1979: The Messinian in Egypt. Proc. Int. Congress Mediterranean Neogene, Athens, Geol. Pays Helleniques, Ann. Hor. Ser., Fasc., **3**, 1083–1090.

Salem A., Williams S., Fairhead D., Smith R., Ravat D., 2008: Interpretation of magnetic data using tilt-angle derivatives. Geophysics, **73**, 1, L1–L10, doi: 10.1190/1.2799992.

Schlumberger C., 1912: Method for determining the composition of the soil by means of electricity (Verfahren zur Bestimmung der Beshaffenheit des Erbodens mittels Elektrizität). German Patent 269,928 (in German).

Shahin H. A. A., Masoud M. S., 2013: Geology and geochemistry of Tertiary basalt in south Wadi Hodein area, South Eastern Desert, Egypt. Arab. J. Geosci., **6**, 8, 2777–2787, doi: 10.1007/s12517-012-0525-6.

Singh U., Sharma P. K., 2022: Study on geometric factor and sensitivity of subsurface for different electrical resistivity Tomography Arrays. Arab. J. Geosci., **15**, 560, doi: 10.1007/s12517-022-09844-3.

Smith N. C., Vozzof K., 1984: Two-dimensional DC resistivity inversion for dipole-dipole data. IEEE Trans. Geosci. Remote Sens., **22**, 1, 21–28, doi: 10.1109/TGRS.1984.350575.

Storemyr P., Heldal T., Bloxam E. G., Harrell J. A., 2003: Widan el-Faras ancient quarry landscape, northern Fayoum Desert, Egypt: Site description, historical significance and current destruction. Report, No. 2003.062, Expert-Center for Conservation of Monuments and Sites, Zürich, 22 p.

Tezel O., Alp H., 2021: High-resolution electrical resistivity imaging of buried grave in Nif (Olympos) Mountain/Izmir. Arab. J. Geosci., **14**, 22, 2357, doi: 10.1007/s12517-021-08741-5.

Trento L. M., Tsourlos P., Gerhard J. I., 2021: Time-lapse electrical resistivity tomography mapping of DNAPL remediation at a STAR field site. J. Appl. Geophys., **184**, 104244, doi: 10.1016/j.jappgeo.2020.104244.

Wenner F., 1912: Characteristics and applications of vibration galvanometers. Proceedings of the American Institute of Electrical Engineers. IEEE, **31**, 6, 1073–1084, doi: 10.1109/PAIEE.1912.6659839.

Wilkinson P. B., Loke M. H., Meldrum P. I., Chambers J. E., Kuras O., Gunn D. A., Ogilvy R. D., 2012: Practical aspects of applied optimized survey design for electrical resistivity tomography. Geophys. J. Int., **189**, 1, 428–440, doi: 10.1111/j.1365-246X.2012.05372.x.